PHYSICAL REVIEW A **82**, 023806 (2010)

Propagation of spatial optical solitons in a dielectric with adjustable nonlinearity

A. Alberucci,[1] A. Piccardi,[1] M. Peccianti,[1,*] M. Kaczmarek,[2] and G. Assanto[1]
[1]*Nonlinear Optics and OptoElectronics Laboratory (NooEL), University ROMA TRE, Via della Vasca Navale 84, I-00146 Rome, Italy*
[2]*School of Physics and Astronomy, University of Southampton, Southampton SO17 1BJ, United Kingdom*

(Received 25 May 2010; published 12 August 2010)

We investigate spatial optical solitons propagating in a medium with a saturable but adjustable nonlinearity and a fixed degree of nonlocality. We employ nematic liquid crystals in a planar cell with optical properties tuned by an external voltage and solitons excited in the near infrared. We also demonstrate soliton self-bending versus excitation due to nonlinear variations in walk-off. A theoretical model accounting for the longitudinal derivatives is employed to compute the refractive index distribution and is found in excellent agreement with the experimental data.

DOI: 10.1103/PhysRevA.82.023806 PACS number(s): 42.65.Tg, 42.65.Jx, 42.70.Df, 78.20.Jq

I. INTRODUCTION

The concept of spatial solitons, nonlinear wave packets preserving their transverse profile while propagating in space, is a unifying one in nonlinear physics [1]. In optics, spatial solitons are formed when linear diffraction is balanced by the lens-like character of either a self-induced index well or a region with enhanced parametric interaction [2–4]. Since the pioneering work by Chiao and collaborators on self-focusing in Kerr media [5], first-order optical bright solitons (i.e., bell-shaped self-localized waves) have been observed via various nonlinear mechanisms such as photorefractivity [6], second-order interactions ($\chi^{(2)}$) [7–11], thermo-optic response [12,13], and reorientation [14–18]. In the latter case, with particular reference to nematic liquid crystals (NLC), several basic functions for all-optical signal processing have been demonstrated, including wavelength-free guidance of low-power signals [14,19], voltage-controlled steering [20,21], deflection by boundaries [22,23], and all-optical logic gating [24–26]. In addition, issues relating to combined variations of nonlinearity and nonlocality [27] and their external control have been addressed in NLC with emphasis on individual soliton (or *nematicon* [28]) propagation and soliton-soliton interactions [22,29–36].

In this paper we investigate, both experimentally and theoretically, solitary wave propagation in NLC with various degrees of nonlinearity; we achieve this nonlinear tuning by modifying the distribution of the molecular director through the application of a low-frequency electric bias in a planar cell as detailed in Ref. [37]. We address the role of nonlinearity in self-trapped beam propagation by analyzing trajectory and waist versus z: These two parameters suffice to describe the evolution of Gaussian-shaped optical solitons in a highly nonlocal dielectric such as NLC [17,38]. In addition, owing to a sample geometry which allows adjusting both linear and nonlinear properties, we observe soliton self-routing via nonlinear changes in walk-off, previously observed under modulational instability [39] and more recently reported with reference to individual nematicons [40] and interacting counterpropagating pairs [41]. Previous experimental observations of soliton self-deflection have been based upon boundary effects on the self-induced waveguides in highly nonlocal media [42,43], photoinduction of an anisotropic charge distribution in photorefractives [44,45] or walk-off mismatch between fundamental and second harmonics in parametric media [9,11,46,47]. At variance with other optical dielectrics often exploited for spatial soliton investigation, such as thermal media where the nonlinearity cannot be easily tuned over a wide range through a macroscopic control parameter [48,49], reorientationally nonlinear NLC allow controlling their molecular response via a low-voltage bias and, additionally, monitoring the soliton evolution through light scattering [14,20], thereby permitting a complete study during propagation. Other examples of externally modulated nonlinearity in physics include, for example, Bose-Einstein condensate solitons by means of Feshbach resonances, where both sign and magnitude of the scattering length, and consequently the potential due to interactions between atoms, can be changed [50,51], and sound propagation in heterogeneous material systems where the nonlinearity can be altered by external magnetic fields [52].

Hereby, we experimentally (as well as theoretically) investigate the role of nonlinearity in the formation and propagation of spatial optical solitons in a reorientational nonlocal medium such as NLC [20,33,53,54]. Noteworthy, at variance with previous work on nematicons [14,17,30], the geometry we employ allows decoupling nonlinearity and nonlocality, the latter being related here to the minimum cell size [23] and independent of the applied voltage. To confirm such features and interpret the data, we develop a two-dimensional (2D) model which is effective in describing the nonlinear optical propagation of a beam in a highly nonlocal medium; we demonstrate that, while the nonlinear refractive index profile in three dimensions is linked to the light intensity through a Poisson-like equation, in an equivalent two-dimensional scenario the pertinent equation is a screened Poisson or Yukawa equation, with screening depending on the minimum cell size. This model can be applied to every highly nonlocal material, including solid [13] and liquid [55] thermo-optic media, atomic vapors [56], and soft matter [57] among others.

---

[*] Present address: Res. Center SMC INFM-CNR, "Sapienza" University, Rome, Italy.

Finally, we explain the observed phenomena with the aid of numerical simulations, addressing for the first time the role of longitudinal nonlocality [58,59] in spatial soliton physics.

II. NONLINEAR OPTICAL PROPAGATION IN NEMATIC LIQUID CRYSTALS

Liquid crystals exhibit properties intermediate between those of solids and liquids. In the nematic phase their elongated organic molecules are distributed in space with a sizable degree of orientational order and a lack of long-range positional order [60], thereby exhibiting uniaxial symmetry, with optic axis (or director) $\hat{n}$ associated to the largest refractive index. Their large birefringence makes NLC an ideal workbench for the investigation of anisotropy and related effects, such as walk-off [20]. Additionally, their anisotropy mediates a strong coupling with electric fields at every frequency, with a torque acting on the molecules to change their orientation and yielding both a large electro-optic response and a large reorientational nonlinearity for extraordinary (*e*-) waves with electric field $\mathbf{E}$ polarized such that $\mathbf{E}\cdot\hat{n}\neq 0$; conversely, ordinary waves (with $\mathbf{E}\perp\hat{n}$) are subjected to the so-called Freedericksz threshold and, at low intensities, have no reorientational effect on the medium [53,54,60,61]. The nonlinearity permits the excitation of solitons at mW power or below [14,25], whereas the nonlocality stemming from the intermolecular links stabilizes $(2+1)D$ solitons [17], otherwise prone to catastrophic collapse in local Kerr media [2,5].

Let us consider a bell-shaped extraordinarily polarized beam propagating forward in NLC (e.g., in a cell as sketched in Fig. 1 or otherwise shaped), with peak wave vector parallel to $\hat{z}$. If the director $\hat{n}$ belongs to the plane yz, its distribution is fully described by the angle $\theta(x,y,z)$ it forms with $\hat{z}$, with θ_0 the orientation in the absence of optical excitation. The elements of the NLC dielectric tensor $\boldsymbol{\epsilon}$ are then $\epsilon_{jk}(\theta)=\epsilon_\perp\delta_{jk}+\epsilon_a n_j n_k$ $(j,k=x,y,z)$, where n_j $(j=x,y,z)$ are Cartesian components of $\hat{n}$ and $\epsilon_\perp$ $(\epsilon_\parallel)$ is the eigenvalue of $\boldsymbol{\epsilon}$ normal (parallel) to the optic axis, with $\epsilon_a=\epsilon_\parallel-\epsilon_\perp$ the dielectric anisotropy. We introduce the walk-off $\delta(\theta)=\arctan(\epsilon_{yz}/\epsilon_{zz})$ and the *e*-refractive index $n_e^2(\theta)=(\epsilon_{yy}-\epsilon_{yz}^2/\epsilon_{zz})/\epsilon_0$. Naming $\theta_b(z)$ the angle θ computed on the beam axis, we define the *e*-wave component of the magnetic field along $\hat{x}$ as $H_x=Ae^{ik_0 n_e^{(b)} z}$, with A the envelope, k_0 the wave vector in vacuum, and $n_e^{(b)}=n_e(\theta_b)$ the refractive index of the carrier. In the paraxial approximation, H_x is the dominant component over those along $\hat{y}$ and $\hat{z}$. In the highly nonlocal case [17], the evolution of H_x along z is ruled by the anisotropic nonlinear Schrödinger equation:

$$2ik_0 n_e^{(b)}\left(\frac{\partial A}{\partial z}+\tan\delta_b\frac{\partial A}{\partial y}\right)+D_y\frac{\partial^2 A}{\partial y^2}+\frac{\partial^2 A}{\partial x^2}+k_0^2\Delta n_e^2 A=0, \tag{1}$$

where $\delta_b=\delta(\theta_b)$, $D_y=[\epsilon_0/\epsilon_{zz}(\theta_b)]n_e^2(\theta_b)$ is the diffraction coefficient in yz and $\Delta n_e^2=n_e^2(\theta)-n_e^2(\theta_b)$ is the nonlinear change in index responsible for light self-confinement. A pointwise reference system xts can be defined at each z by rotating xyz by an angle δ_b around $\hat{x}$; in this moving frame in yz, $\hat{s}$ is the "local" Poynting vector and the electric field can be expressed by $E_t\approx(\frac{\partial H_x}{\partial z}+\tan\delta_b\frac{\partial H_x}{\partial y})/(-i\omega\epsilon_0 n_e^2\cos\delta_b)$, with ω the angular frequency. In the paraxial regime $E_t\approx-[Z_0/(n_e^{(b)}\cos\delta_b)]H_x$, with Z_0 the vacuum impedance.

To obtain the θ-dependent parameters appearing in Eq. (1) we need to calculate the spatial distribution of θ (i.e., the director angle) via a reorientation equation which, based on our previous assumptions and the single-constant approximation for elastic NLC deformations [53,54,61], reads

$$\nabla^2\theta+\gamma|E_t|^2\sin[2(\theta-\delta_b)]=0, \tag{2}$$

with $\gamma=\epsilon_a/(4K)$ and K the elastic (Frank) constant [60]. Since the derivatives along z are included in Eq. (2), we are accounting for nonlocality also along the propagation direction, at variance with models previously employed for spatial solitons [13,17,20,57,62–68]. We set $\theta=\theta_0+\psi$, with θ_0 the director angle fixed by the boundary conditions [60] and ψ the light-induced reorientation. Assuming θ_0 to be homogeneous across the NLC volume, Eq. (2) gives

$$\nabla^2\psi+\gamma|E_t|^2\sin[2(\theta_0+\psi-\delta_b)]=0, \tag{3}$$

with ψ zero at the NLC boundaries owing to strong anchoring [60]. Equation (2) [or equivalently Eq. (3)] nonlinearly links the intensity $I\propto|A|^2$ of the electromagnetic wave to the optically induced perturbation ψ. Therefore, it is not solvable through the Green function formalism, but retains its validity for every regime of the reorientational nonlinearity, including saturation (when $\hat{n}$ becomes nearly parallel to E_t [60]) and nonlinear changes in walk-off [27]. In the limit $\psi\ll\theta_0$, Eq. (3) reduces to the linear Poisson equation because reorientation in the second term can be neglected [43]. The solutions of this linearized version of Eq. (3) depend on the specific geometry, the latter defining—in turn—a specific Green function [69]: otherwise stated, the nonlocality varies with the cell geometry. As it can be easily shown with a perturbative approach [43], such considerations hold valid in every applicable regime of Eq. (3).

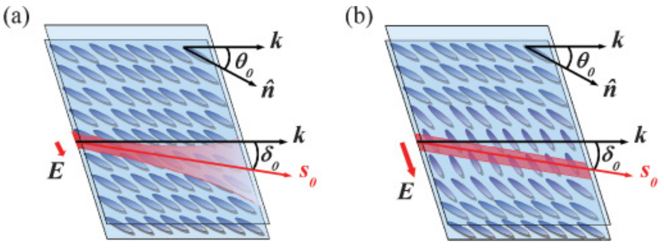

FIG. 1. (Color online) Sketch of a light beam traveling in a planar (unbiased) NLC cell, the latter unlimited in the plane yz and of thickness L along x. The anchoring conditions at the boundaries (glass interfaces) induce a homogeneous director distribution, with $\hat{n}\cdot\hat{z}=\cos\theta_0$ and $\hat{n}\cdot\hat{x}=0$. (a) A low-power *e*-polarized Gaussian beam launched with wave vector parallel to z diffracts, its Poynting vector walking-off at an angle δ_0 with respect to z; (b) an *e*-beam of sufficient power induces self-confinement but no changes in walk-off: the soliton propagates along the previous (linear) Poynting vector.

Let us now discuss the nonlinear response in the low-perturbation regime. As clear from Eq. (1), $\Delta n_e^2 = \Delta n_e^2(|E_t|^2)$; consistently with our assumptions, we write

$$\Delta n_e^2 = 2n_e(\theta_0)\Delta n_e = 2\psi\ (|E_t|^2)n_e(\theta_0)\frac{\partial n_e}{\partial \theta}\bigg|_{\theta=\theta_0}, \tag{4}$$

where $\frac{\partial n_e}{\partial \theta} = \frac{\sin(2\theta)}{2}(\frac{1}{\epsilon_\perp} - \frac{1}{\epsilon_\parallel})(\frac{\cos^2\theta}{\epsilon_\perp} + \frac{\sin^2\theta}{\epsilon_\parallel})^{-3/2}$ and ψ is given by

$$\psi = \gamma \sin[2(\theta_0 - \delta_0)] \times \iiint G(x,y,z,x',y',z')|E_t(x',y',z')|^2 dx'dy'dz', \tag{5}$$

in which we set $\delta_0 = \delta(\theta_0)$ and accounted for the finiteness of the cell [23]; hence, for an assigned G, it is natural to introduce a figure of nonlinearity n_2 as

$$n_2(\theta_0) = 2\gamma \sin[2(\theta_0 - \delta_0)]n_e(\theta_0)\ \frac{\partial n_e}{\partial \theta}\bigg|_{\theta=\theta_0}, \tag{6}$$

which yields

$$\Delta n_e^2 = n_2(\theta_0)Pg(x,y,z), \tag{7}$$

having introduced the normalized field u as $E_t = \sqrt{P}v$ and $g = \iiint G|v|^2dx'dy'dz'$.

Noteworthy, by using $n_e(\theta_0)\tan\delta_0 = \partial n_e/\partial\theta|_{\theta=\theta_0}$ we find for n_2 the alternative expression,

$$n_2(\theta_0) = 2\gamma \sin[2(\theta_0 - \delta_0)]n_e^2(\theta_0)\tan\delta_0, \tag{8}$$

The coefficient γ depends on material parameters and is zero for null birefringence ($\epsilon_a = 0$) or when the intermolecular forces are very high ($K \to \infty$). The two remaining terms in Eq. (6) depend on θ_0, therefore, n_2 can be tuned by changing the distribution of the director $\hat{n}$ at rest. In particular, n_2 is zero when either $\theta_0 = 0$ owing to the Freedericksz threshold [60] or $\theta_0 = \pi/2$ owing to saturation as E_t and $\hat{n}$ are parallel to one another. Figure 2 shows plots of n_2 versus θ_0: for a low anisotropy, the nonlinearity reaches its maximum for θ_0 slightly larger than $\pi/4$, with a moderate asymmetry with respect to the peak due to uniaxiality. For large ϵ_a, n_2 becomes markedly asymmetric [Fig. 2(a)] with a maximum monotonically increasing with ϵ_a [Fig. 2(d)]. Clearly, in the nonperturbative regime each angle θ_0 corresponds to a distinct saturating behavior because of the sine term in Eq. (6), as we shall prove by numerically solving the system of Eqs. (1) and (3).

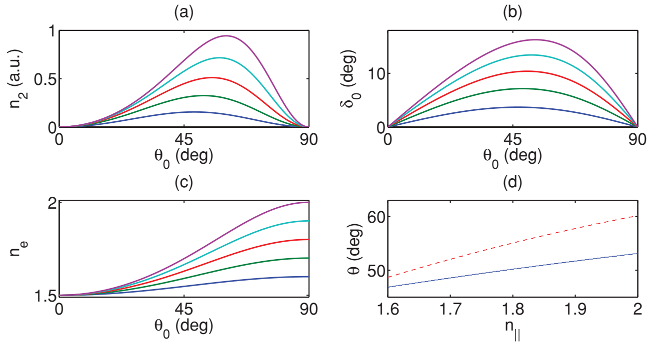

FIG. 2. (Color online) Plots of (a) nonlinearity n_2, (b) walk-off δ_0, and (c) refractive index $n_e(\theta_0)$ versus director angle θ_0 at rest; each line corresponds to a different value of $n_\parallel = \sqrt{\epsilon_\parallel/\epsilon_0}$, from 1.6 (bottom line) to 2 (top line) in 0.1 steps. (d) The dotted (solid) line is θ_0 versus $n_\parallel$ corresponding to the maximum of n_2 (maximum of δ_0). Here, $n_\perp = \sqrt{\epsilon_\perp/\epsilon_0} = 1.5$.

The NLC nonlocal response, in contrast to local Kerr [70], does not impose a critical power for soliton formation [20,57]; hence, self-guided waves exist and are stable over a large range of intensities (infinitely extended in unbounded media) [18,38,66]. Owing to the continuous interplay between light spreading via diffraction and self-focusing via reorientation, soliton waist in NLC changes versus propagation (i.e., nematicons breathe according to excitation power and initial spot size [18,38,71]). Moreover, due to the high nonlocality, soliton profiles are nearly Gaussian, which makes the knowledge of (just) their waist and position along z sufficient to fully describe their propagation [17,23].

To derive soliton trajectories we define the averaged position defined as $\boldsymbol{r}_b(z) = \iint \boldsymbol{r}|A|^2dx\,dy/\iint|A|^2dx\,dy$ ($\boldsymbol{r} = x\hat{x} + y\hat{y}$). From the Ehrenfest's theorem applied to Eq. (1) we get the evolution equation along z [72]:

$$\frac{d^2\boldsymbol{r}_b}{dz^2} = \frac{n_e(\theta)}{n_e^2(\theta_b)}\nabla_{xy}n_e(\theta)\bigg|_{\boldsymbol{r}_b} + \frac{\partial \tan\delta_b}{\partial z}\hat{y}, \tag{9}$$

where $\nabla_{xy} = \hat{x}\partial/\partial x + \hat{y}\partial/\partial y$ and we compute the right-hand side in the highly nonlocal limit. Finally, we calculate the waist w in ξ ($\xi = x,y$) as $w = 2\sqrt{\iint(\xi - \xi_b)^2|A|^2dx\,dy/\iint|A|^2dx\,dy}$.

III. PLANAR CELLS

Let us consider planarly aligned NLC in flat and planar sandwich-like cells (see Fig. 1), infinitely extended in yz and of thickness L along x, with $x = 0$ at the bottom boundary. We can write

$$\psi(x,y,z) = \sum_{n=1}^{\infty}\psi_n(y,z)\sin\left(\pi n\frac{x}{L}\right). \tag{10}$$

Substituting Eq. (10) into Eq. (3) and considering a highly nonlocal response we obtain

$$\nabla_{yz}^2\psi_n - \left(\frac{\pi n}{L}\right)^2\psi_n + \gamma\sin[2(\theta_0 + \psi - \delta_b)]|_{x_b}I_n(y,z) = 0, \tag{11}$$

for every positive integer n, having exploited the orthogonality of sine functions and let $I_n = (2/L)\int_0^L|E_t|^2\sin(\pi nx/L)dx$. Equation (11) is an infinite set of screened Poisson equations, with screening lengths $L_n = L/(n\pi)$; their Green functions are modified Bessel functions of the second kind $K_0(\rho/L_n)$, with $\rho = \sqrt{(y-y')^2 + (z-z')^2}$. Thus, the nonlinear perturbation ψ is

$$\psi(x,y,z) = \frac{\gamma}{2\pi}\sum_{n=1}^{\infty}\sin\left(\pi n\frac{x}{L}\right) \times \iint K_0(\rho/L_n)\sin[2(\theta_0 + \psi - \delta_b)]|_{x_b}I_n(y',z')dy'dz', \tag{12}$$

with nonlinearity expressed by ψ on the right-hand side.

For a small perturbation (i.e., small ψ), $g(x,y,z) = \frac{1}{2\pi P}\sum_{n=1}^{\infty}\sin(\pi n\frac{x}{L})\iint K_0(\rho/L_n)I_n(y',z')dy'dz'$ and the Green function is

$$G(x,x',\rho) = \frac{1}{2\pi}\sum_{n=1}^{\infty}K_0(\rho/L_n)\sin\left(\pi n\frac{x}{L}\right)\sin\left(\pi n\frac{x'}{L}\right). \tag{13}$$

The shape of the three-dimensional (3D) Green function above depends on x' owing to the finite x boundaries which break the translational symmetry [23,42,43]. Equation (13) also implies a nonlocality determined by $L_1 = L/\pi$, consistently with Ref. [43] where the case $\partial^2\psi/\partial z^2 = 0$ was addressed.

The fully nonlinear case in the highly nonlocal limit can be dealt with by taking the nonlinear perturbation ψ [on the RHS of Eq. (12)] on beam axis, (i.e., $x = x_b$ and $y = y_b$). Equation (12) can be solved iteratively as a 3D Poisson equation, taking a forcing term $\sin\{2[\theta_0 + \psi_b(z) - \delta_b(z)]\}I_n(y,z)$, with $\psi_b(z) = \psi|_{x_b,y_b}$. Thus, the degree of nonlocality is always ruled by Eq. (13), even though the perturbation amplitude has a nonlinear dependence on soliton power due to the sine term [23]. According to Eq. (13), the director distribution does not vary on length scales much smaller than L in any direction, in contrast to the case when the second derivatives along z are neglected, that is, without (low-pass) spatial filtering of the director changes along z. Remarkably, this result holds valid for an arbitrarily highly nonlocal nonlinearity in a finite geometry (along at least one direction), provided the width of the Green function is comparable with the smallest size.

IV. TWO-DIMENSIONAL MODEL

Equations (1)–(11) completely model the 3D propagation of spatial solitons in NLC. Since we are mainly interested in soliton propagation in the cell midplane $x = L/2$ (i.e., $x_b = L/2$ for every z), where the forces exerted by the boundaries balance out [23], it is convenient to resort to a simpler 2D description which encompasses all the main features of the 3D model in the previous section.

Setting $A = X(x,z)u(y,z)$ in (1) and integrating along x yields

$$2ik_0n_e^{(b)}\left(\frac{\partial u}{\partial z} + \tan\delta_b\frac{\partial u}{\partial y}\right) + D_y\frac{\partial^2 u}{\partial y^2} + k_0^2\left(\Delta n_e^2\right)_{eq}u = 0, \tag{14}$$

where we defined $(\Delta n_e^2)_{eq} = \int_{-\infty}^{\infty}X\Delta n_e^2dx/\int_{-\infty}^{\infty}Xdx$. In the highly nonlocal limit we use $(\Delta n_e^2)_{eq} = \Delta n_e^2|_{x=L/2}$ in Eq. (11) and obtain $I_n(y,z) = |u(y,z)|^2(2/L)\int_0^L|X|^2\sin(\pi nx/L)dx = I_n^x(z)I_{yz}(y,z)$, with $I_n^x(z) = (2/L)\int_0^L|X|^2\sin(\pi nx/L)dx$ and $I_{yz} = |u|^2$. Therefore, for reorientation in the midplane,

$$\psi(x = L/2,y,z) = \sum_{n=1}^{\infty}\sin(\pi n/2)I_n^x(z)\psi_n^{2D}(y,z), \tag{15}$$

with each $\psi_n^{2D}(y,z)$ satisfying the corresponding equation:

$$\nabla_{yz}^2\psi_n^{2D} - \left(\frac{\pi n}{L}\right)^2\psi_n^{2D} + \gamma\sin[2(\theta_0 + \psi - \delta_b)]|_{y_b}I_{yz} = 0. \tag{16}$$

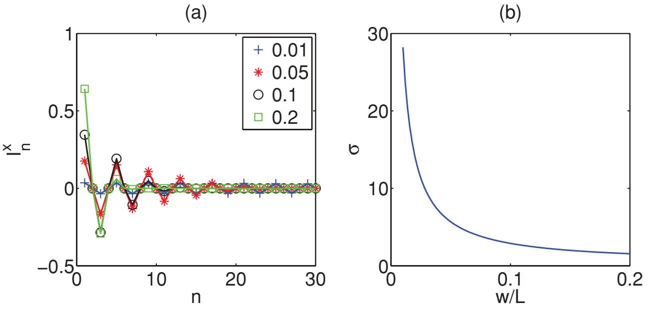

FIG. 3. (Color online) (a) Values of I_n^x for $w/L = 0.01$ (blue crosses), 0.05 (red stars), 0.1 (black circles), and 0.5 (green squares). (b) σ versus normalized waist w/L; as expected, σ is maximum for small waists and tends to unity for large spot sizes.

If $X(x)$ is even with respect to $x = L/2$ [i.e. $X(L/2 - a) = X(L/2 + a)$ with $a < L/2$] with a single-hump profile, for odd n only the ψ_n^{2D} are nonzero, with $\sin[\pi(2m+1)/2]I_{2m+1}^x(z) = |I_{2m+1}^x(z)|\forall\, m \in \mathbb{N}$. Therefore, to a first approximation, nonlinear optical propagation in the midplane is described by the two-dimensional model Eqs. (14) and (16), the latter taken for $n = 1$ with an equivalent intensity I_{eq} such that $I = \sigma I_{\text{eq}}$, with $I = n_e^{(b)}/(2Z_0\cos\delta)|E_t|^2$ the actual beam intensity and σ a fit parameter. We estimate σ using Eq. (15); assuming equal amplitudes of all ψ_{2m+1}^{2D}, we get

$$\sigma \approx \sum_{m=0}^{\infty}|I_{2m+1}^x|/|I_1^x|. \tag{17}$$

Thus, it must be $\sigma > 1$. Figure 3 shows σ as computed with Eq. (17) for a Gaussian profile along x, that is, $X(x) = \exp[-(x - L/2)^2/w^2]$; in this case $I_n^x(x/L) \approx (\sqrt{\pi}w/L)\sin(\pi n/2)e^{-(\frac{\pi nw}{2L})^2}$ [23].

We numerically integrated our model Eqs. (14) and (16) with an anisotropic beam propagator, using the beam profile to calculate the director distribution in the plane yz via an over-relaxed Gauss-Seidel scheme and iterating until convergence [73]. For the boundaries in θ we assumed the nonlinear changes at the grid edges to be zero (i.e., $\theta = \theta_0$). The grid size along y was such that its minimum distance from the beam exceeded the nonlocality L. Analogously, we used a grid along z twice wider than the propagation distance (chosen to be 1.5 and 3 mm, respectively). Finally, in Eq. (14) we inserted a loss term $2ik_0n_e^{(b)}\alpha u$ to better model the experimental results; losses in our samples were mainly due to Rayleigh scattering [60], measured to amount to $\alpha \approx 5\ \text{cm}^{-1}$ [for $P(z) = P(z = 0)e^{-2\alpha z}$].

Figures 4–6 show the results of our simulations for a Gaussian input of waist 5 μm: in the linear regime the beam diffracts owing to negligible reorientation. For each θ_0 the beam diffracts with a specific divergence due to $D_y = D_y(\theta_0)$ in Eq. (14) and a distinct walk-off (see Figs. 5 and 6, respectively), in agreement with Fig. 2(b). As power increases, the beam undergoes self-focusing (see the waist trend in Fig. 5) until a soliton eventually forms; the effect is stronger for $\theta_0 = 40°$ and $\theta_0 = 50°$, as predicted in Sec. II. We also note that self-focusing at high powers is markedly more asymmetric

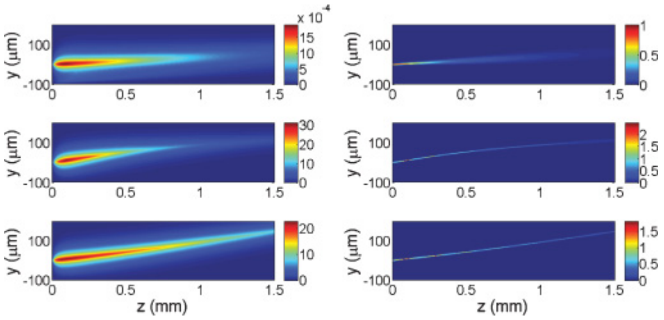

FIG. 4. (Color online) Simulated nematicon evolution in the plane yz for $\theta_0 = 10^\circ$ and $P_{\mathrm{eq}} = 1\ \mu$W (first row), $\theta_0 = 10^\circ$ and $P_{\mathrm{eq}} = 5$ mW (second row), $\theta_0 = 50^\circ$ and $P_{\mathrm{eq}} = 5$ mW (third row). Left and right columns display perturbation ψ (in degrees) and intensity $|u|^2$ (in arbitrary units), respectively. Here, $L = 100\ \mu$m, $\sqrt{\epsilon_\perp/\epsilon_0} = 1.5$, and $\sqrt{\epsilon_\parallel/\epsilon_0} = 1.7$, corresponding to the NLC E7 at $\lambda = 1064$ nm.

with respect to $\theta_0 = \pi/4$, if compared with the theoretical predictions stemming from Eq. (6); this is easily explained by saturation in the reorientational response, previously neglected in expression (6) which was derived for low reorientation (see Sec. II).

The numerical results demonstrate that nematicon trajectories depend on power via nonlinear changes in walk-off. In fact, from Eq. (9) and since no *effective* index gradient acts on the beam when launched in the midplane $x = L/2$ [43], the direction of the local Poynting vector is determined by the walk-off $\delta_b(z)$ which depends on $\theta_b(z) = \theta_0 + \psi_b(z)$ and, thus, on optical reorientation ψ_b. For $z \gg \alpha^{-1}$, the soliton angle with respect to z is given by the linear $\delta_0(\theta_0)$ owing to the exponential decay of ψ along z, as confirmed by Fig. 6 where it is apparent that the soliton trajectories in $z = 1.5$ mm are parallel regardless of the power. Furthermore, the variations in δ_b at low powers follow Fig. 2(b): for $\theta_0 < 40^\circ$ ($\theta_0 > 40^\circ$) the walk-off increases (reduces) with excitation. Both sign and magnitude of the nonlinear changes match the theoretical predictions: the soliton displacement (Fig. 6) is maximum for θ_0 close to either 0 or $\pi/2$, but small for $\theta_0 = \pi/4$; hence, the displacement has an opposite trend with respect to the nonlinear Kerr figure [see Fig. 2(a)]. This counterintuitive result stems from the interplay between nonlinearity and walk-off sensitivity versus θ.

V. GEOMETRY OF THE TUNABLE SAMPLE

The nonlinearity in NLC depends on the rest angle of the director. In standard planar NLC cells [20] the director distribution in the absence of external excitation is determined by anchoring at the glass-NLC interfaces. A low-frequency voltage bias across x produces an index well across the NLC thickness, causes solitons to propagate out of the plane yz [74], and changes the effective nonlocality [18]. In our experiments, conversely, we used a planar cell as in Ref. [37], where an electric bias can alter the NLC conditions at the boundaries. Two interdigitated comb electrodes in transparent indium tin oxide (ITO) are deposited on each of the two glass-NLC interfaces (parallel to yz) (see Fig. 7), with comb-teeth orthogonal to z; in the plane yz, adjacent teeth of distinct electrodes are spaced by $\Lambda - l$ along z and extend l in width. A voltage V applied between them originates an alternating electric field E_{LF} with period 2Λ along z. For $\Lambda \ll L$, the dominant component of E_{LF} is along z and molecular reorientation takes place in the plane yz; thus, the dielectric properties of the NLC are simply determined by the angle θ of the director with z, governed by

$$\frac{\partial^2\theta}{\partial x^2} + \frac{\partial^2\theta}{\partial z^2} - \gamma_{LF}\sin(2\theta)|E_{LF}|^2 = 0. \qquad (18)$$

Due to anchoring, we take $\theta = \theta_B$ in both $x = 0$ and $x = L$ and apply periodic boundary conditions along z, as θ is periodic with the electric field E_{LF}^2 in the limit of infinitely extended electrodes along z with period Λ. Since $\theta(x = L/2 - a, z) = \theta(x = L/2 + a, z)$ we study $\theta(x,z)$ in the range $z \in [0\ \ \Lambda]$ with $x \in [0\ \ L/2]$. At low reorientation, Eq. (18) can be solved with the Green function (G) formalism, with $G(x,x',|z-z'|) = -\sum_{m=1}^{\infty}\frac{1}{\pi m}\sin(\pi m x'/L)\sin(\pi m x/L)e^{-(\pi m|z-z'|/L)}$ [23]. To find an expression for E_{LF} we take $E_{LF} = V/(\Lambda - l)$ in $x = 0$ $(x = L)$ between the electrodes and zero below or above them; we assume an exponential decay $e^{-\kappa x}$ along x, with κ a fit parameter describing the coupling between the NLC molecules and the external bias. Thus,

$$|E_{LF}| = \frac{V}{\Lambda - l}\mathrm{rect}_{\Lambda-l}[z - (\Lambda - l)/2]e^{-\kappa x}, \qquad (19)$$

where $\mathrm{rect}_d(z)$ is equal to 1 for $z \in (-d/2\ \ d/2)$, 0.5 in $z = \pm d/2$, and zero elsewhere.

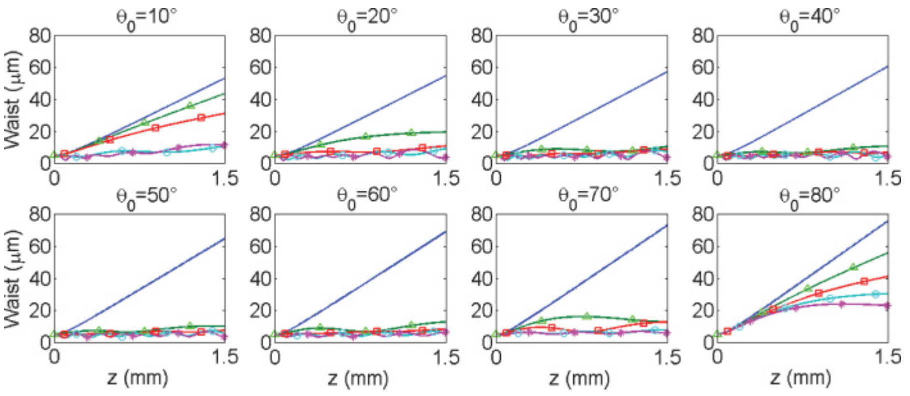

FIG. 5. (Color online) Beam waist versus input power P_{eq} (see the text for definition) at rest angles θ_0 ranging from 10° to 80°. Blue solid line without symbols, green line with triangles, red line with squares, cyan line with circles, and magenta line with asterisks correspond to $P_{\mathrm{eq}} = 1\ \mu$W, 500 μW, 1 mW, 3 mW, and 5 mW, respectively.

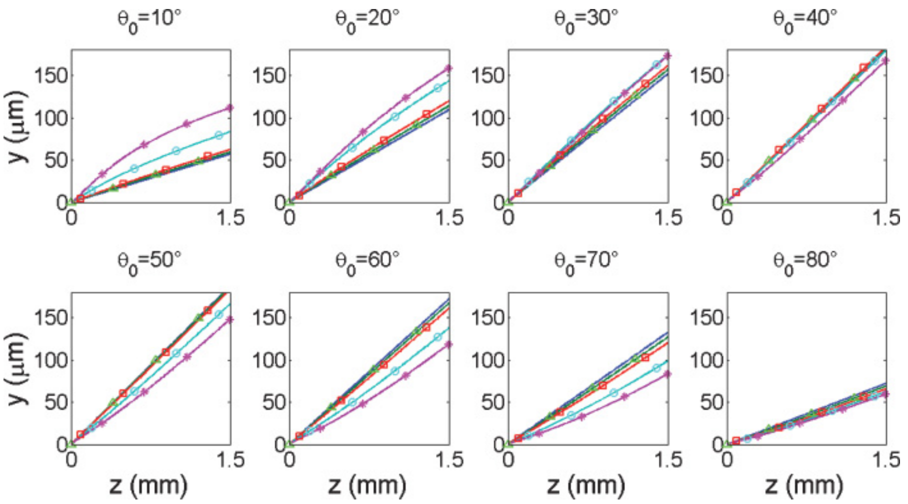

FIG. 6. (Color online) Beam trajectory versus input power P_{eq} at rest angles θ_0 ranging from 10° to 80°. Blue solid line without symbols, green line with triangles, red line with squares, cyan line with circles, and magenta line with asterisks correspond to $P_{\mathrm{eq}} = 1\ \mu$W, 500 μW, 1 mW, 3 mW, and 5 mW, respectively.

Defining the electric perturbation as $\Delta\theta(x,z) = \theta(x,z) - \theta_B$, Eq. (18) provides $\Delta\theta = -\gamma_{LF}\sin(2\theta_B)\iint |E_{LF}(x',z')|^2 G(x,x',|z-z'|)dx'dz'$. We find

$$\Delta\theta = -\gamma_{LF}\sin(2\theta_B)\frac{2V^2}{(\Lambda - l)^2} \times \sum_{p=-\infty}^{\infty}\sum_{m=0}^{\infty}\frac{\sin[\pi(2m+1)x/L]}{\pi(2m+1)}Q(z,p,2m+1)R(2m+1), \tag{20}$$

being

$$Q(z,p,m) = \int_{p\Lambda}^{(p+1)\Lambda-l} e^{-\pi m|z-z'|/L}dz', \tag{21}$$

$$R(m) = \int_0^{L/2}\sin(\pi m x'/L)e^{-2\kappa x'}dx'. \tag{22}$$

Solutions of integrals (21) and (22) are reported in Appendix.

With reference to the experimental parameters $\theta_B = 80°$, $L = 100\ \mu$m, $\Lambda = 30\ \mu$m, $l = \Lambda/2$, and the (commercial) NLC mixture E7, Fig. 8 displays the computed $\Delta\theta$ for various κ and low reorientation. For each voltage the induced reorientation is larger for smaller κ, owing to an increased coupling between field and NLC, and the overall shape of $\Delta\theta$ depends on κ, as well: for rapidly decaying electric fields (i.e., large κ) θ has marked peaks and dips versus z corresponding to the ITO pattern; for lower κ the nonlocality smoothes out the $\Delta\theta$ profile. Around the midplane $x = L/2$ θ is flat and determined by the bias V, as the intermolecular forces stretch the effects of E_{LF} to distances comparable with the nonlocal range L. In essence, the cell behaves as a planar system with anchoring θ_0 controlled by V, that is, an ideal experimental setting for investigating spatial solitons versus nonlinearity (i.e., Kerr figure).

Our considerations above apply to small $\Delta\theta$, when Eq. (18) can be linearized. For large $\Delta\theta$, conversely, saturation due to the sine term becomes relevant. To address the latter and

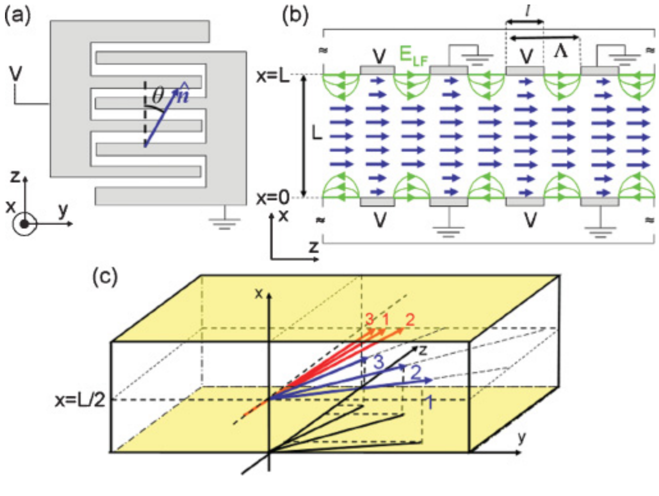

FIG. 7. (Color online) (a) Top and (b) side views of the cell used in this work. The blue arrows represent the molecular director. In (b) the director distribution induced by the bias V applied to the interdigitated electrodes is sketched; the profile is inhomogeneous close to the interfaces in $x = 0$ and $x = L$, and homogeneous in the bulk of the NLC, with angle θ depending on V. The field lines of the low-frequency electric field E_{LF} (green lines) are drawn qualitatively; the glass thickness is not in scale with L and the director is not indicated when it overlaps with E_{LF} for the sake of clarity. (c) In-plane soliton steering: the red lines represent the soliton trajectories versus power and indices 1, 2, and 3 correspond to increasing V (see Ref. [37]).

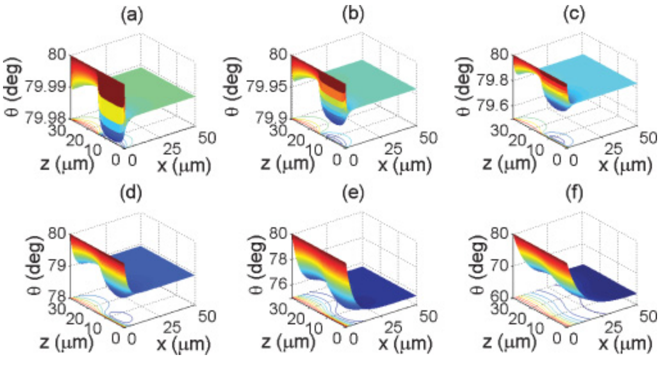

FIG. 8. (Color online) Plots of $\Delta\theta$ versus z and x computed from Eq. (20) for (a) $\kappa = 2\times10^6\ \mathrm{m}^{-1}$, (b) $1\times10^6\ \mathrm{m}^{-1}$, (c) $5\times10^5\ \mathrm{m}^{-1}$, (d) $2\times10^5\ \mathrm{m}^{-1}$, (e) $1\times10^5\ \mathrm{m}^{-1}$, and (f) $5\times10^4\ \mathrm{m}^{-1}$. Here the applied bias is $V = 2$, the electrodes extend from $z = 0$ to $z = 15\ \mu$m, $L = 100\ \mu$m, $K = 12\times10^{-12}\ N$ and $\epsilon_{LF} = 1.25\times10^{-10}\ \mathrm{Fm}^{-1}$.

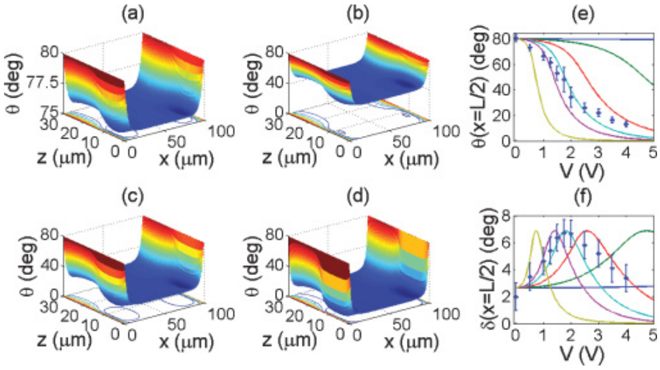

FIG. 9. (Color online) $\Delta\theta$ profiles computed with Eq. (18) for $\kappa = 1.3 \times 10^5\ \text{m}^{-1}$ and (a) $V = 1$ V, (b) 2 V, (c) 3 V, and (d) 5 V, respectively. (e) θ in the midplane $x = L/2$ and (f) corresponding walk-off at $\lambda = 1064$ nm versus bias V. In (e) and (f) the dots are experimental data and each line corresponds to a different κ; from left to right $\kappa = 5 \times 10^4$, 1.3×10^5, 2×10^5, 4×10^5, and $2 \times 10^6\ \text{m}^{-1}$, respectively.

fully compare theory and experiments, we solved Eq. (18) using an over-relaxed Gauss-Seidel scheme [73]. The results are shown in Fig. 9: from (a)–(d), it is apparent that the θ profile is perfectly consistent with the predictions of Eq. (20), even for voltages well beyond the low reorientation limit. This is better understood by solving Eq. (18) with a perturbative approach, as it can be proven to be equivalent to an infinite set of Poisson equations and therefore share the same Green function [43]. The effects of saturation can be addressed numerically: Fig. 9(e) graphs the midplane NLC reorientation for various κ; for low κ the curve resembles the Freedericksz transition [60], whereas for high κ the reorientation is smoother due to a smaller coupling between E_{LF} and the NLC, with a much lower slope for $\kappa = 2 \times 10^6\ \text{m}^{-1}$. Finally, Fig. 9(f) displays the walk-off corresponding to reorientation dynamics in Fig. 9(e): by the applied bias V it is possible to angularly steer solitons over a range as large as 7°, the sensitivity with V being maximum for strong coupling.

VI. EXPERIMENTAL RESULTS

An infrared beam from a Nd:YAG laser source operating at $\lambda = 1.064\ \mu$m was focused at the cell input with a waist of about $w_0 = 5\ \mu$m; its evolution in the plane yz was monitored by collecting the out-of-plane scattered light with a microscope objective and a CCD camera [14]. We studied nonlinear propagation for powers ranging from 1 to 10 mW and by varying the applied bias, that is, the effective nonlinearity (see expression of n_2 in Sec. II and discussion therein), but keeping the nonlocality constant (the latter related to the cell size L). Figure 10 displays the beam evolution in yz for various voltages V and input powers P. At low powers the beams (launched with wave vector parallel to z) propagate straight along their linear walk-off determined by V. Figure 9(f) graphs the measured walk-off versus V, whereas Fig. 9(e) shows the corresponding angle between wave vector and director in the midplane. At each V the sample effectively behaves as a standard cell [20] with anchoring at $\theta_0(V)$ [Fig. 9(e)] [37]. Since the agreement between predicted and measured walk-off is excellent for $V < 2V$, from our data on soliton walk-off versus voltage V we can estimate $\kappa = 2 \times 10^5\ \text{m}^{-1}$ [see Fig. 9(f)]. For larger biases the computed walk-off is smaller than measured due to the approximated distribution of the electric field with no x components.

Figure 11 plots the beam waist versus excitation and voltage. At $\theta_0 = 80°$ (i.e., no voltage), the beam diffracts for $P = 1$ mW (waist quasilinearly growing with z), whereas it weakly self-focuses for P up to 6 mW; for $P = 8$ mW self-focusing is witnessed by the reduction in beam waist for large z; for $P = 10$ mW the waist in $z = 0$ and $z = 1.5$ mm is the same, indicating the formation of a self-confined breather [18,38]. At $\theta_0 = 60°$ the nonlinearity gets larger and self-confinement occurs for $P = 2$ mW, with a breathing

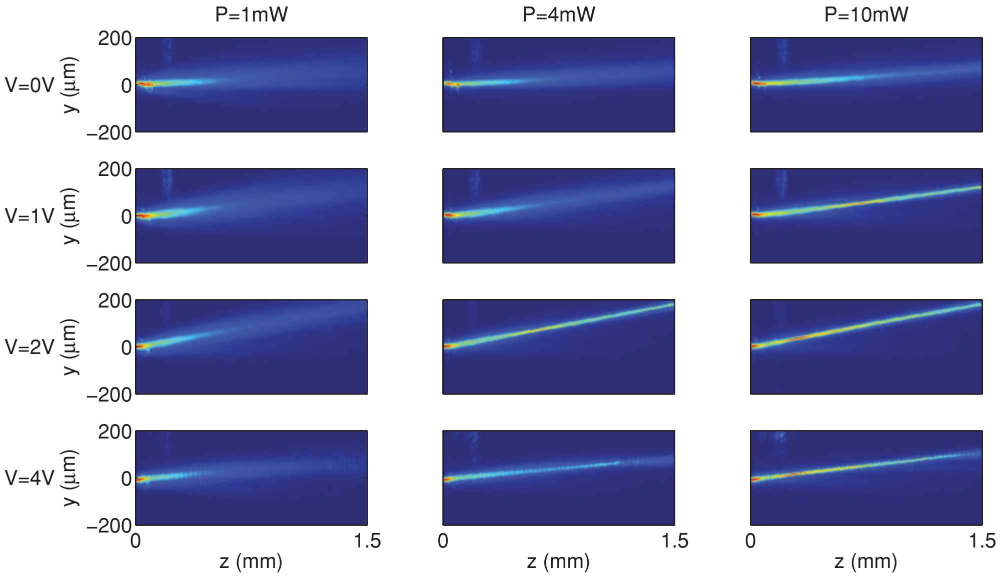

FIG. 10. (Color online) Acquired evolution of an extraordinary beam at $\lambda = 1064$ nm for various input powers and biases. For $V = 4$ V we observed oscillations along z with the same periodicity of the electrodes and attributed them to the effect of the transition zone near the cell edges (Fig. 9).

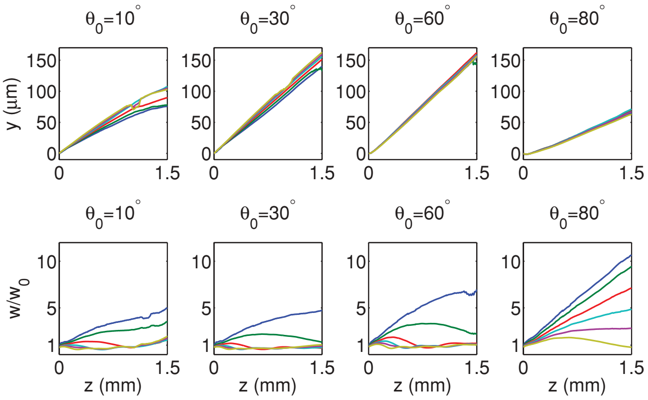

FIG. 11. (Color online) (First row) Measured beam trajectories in the plane yz for various θ_0 (legends) and powers; powers are $P = 1$ (blue line), 2 (green), 4 (red), 6 (purple), 8 (cyan), and 10 mW (yellow), from bottom to top for $\theta_0 = 10^\circ$ and $\theta_0 = 30^\circ$, and from top to bottom for $\theta_0 = 60^\circ$ and $\theta_0 = 80^\circ$. (Second row) Corresponding evolution of beam waist versus z for the same set of powers. The power corresponding to each line can be inferred by the fact that lower waists correspond to larger power, if propagation close to the entrance (i.e., on a single breathing period) is considered.

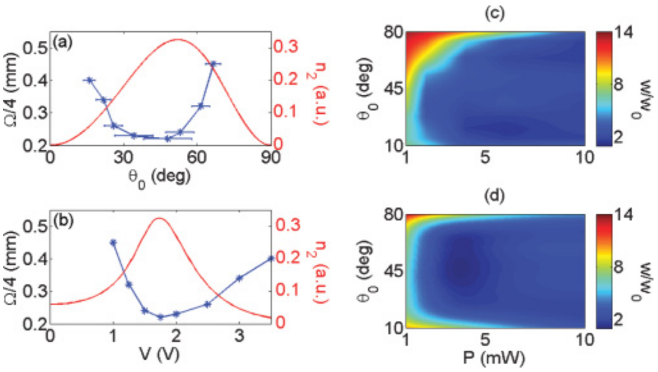

FIG. 12. (Color online) (a) and (b) Measured Ω (blue line with symbols) and n_2 [red solid line; see Eq. (6) for a definition] for $P = 4$ mW and versus (a) θ_0 and (b) V, respectively. Error bars are derived from Fig. 9(e). (c) Experimental and (d) numerically averaged waist along z versus power P and $\theta_0(V)$. The best fit is obtained for $\sigma = 5$ (see Sec. IV). Slight discrepancies are due to scattering losses, taken constant in the numerical simulations whereas they actually depend on $\theta_0(V)$ [60].

period continuously reducing from 2 mm to 250 μm as the excitation goes from 4 to 10 mW; the waist $w(z)$ oscillates around a mean value comparable with the input spot size. At $\theta_0 \simeq 40^\circ$ self-focusing becomes appreciable for powers as low as 1 mW and the breathing period reaches a minimum of about 120 μm for $P = 10$ mW as the nonlinearity becomes the largest. If bias is further increased past the maximum in n_2, then the waist evolves with an opposite trend, in agreement with the bell-shaped curve in Fig. 2(a); the breathing period Ω becomes longer (for a fixed power) as the nonlinearity decreases, with diffraction becoming dominant for $\Omega \to \infty$.

The period Ω is a scalar quantity well suited for the (indirect) evaluation of the nonlinearity. However, since scattering reduces the optical power in propagation and distorts the sinusoidal behavior predicted in the ideal limit (see Sec. II and simulations therein) [18,38], we evaluated Ω as four times the distance z where the waist takes its first maximum. For a fixed input power $P = 4$ mW, Figs. 12(a) and 12(b) plot Ω versus θ_0 and voltage V, respectively: Ω decreases from 1.8 to 0.9 mm as V goes from 0 to $2V$, reaching its minimum for the latter value (for $\theta_0 \simeq 45^\circ$ the nonlinearity is maximum) and eventually increasing again for larger V. The breathing period is longer at higher θ_0, at variance with what is expected from the theoretical expression of n_2: this is a consequence of saturation, more relevant for θ_0 closer to $\pi/2$ and not considered in deriving Eq. (6). Saturation effects are more apparent in Figs. 12(c) and 12(d), graphing both numerical and experimental z-averaged waists: the solitons are wider for θ_0 close to $\pi/2$ (i.e., low V) (see results for $\theta_0 = 80^\circ$ and $\theta_0 = 10^\circ$). Figures 12(c) and 12(d) show an excellent agreement between simulations and experiments with a fit-coefficient $\sigma = 5$; the latter is consistent with the predictions in Sec. IV. From the relationship between θ and δ [see Fig. 2(b)], the largest changes in walk-off (for low powers) are expected for θ close to either 0 or $\pi/2$; experimentally, we verified that indeed the largest soliton self-deflections occur for either θ_0 close to 0° or 90° (Fig. 11), although the explored range of powers was limited in order to prevent the insurgence of time-dependent instabilities; the upper bound of 10 mW in the experiments ensured reproducible results at each voltage.

VII. CONCLUSIONS

We have introduced, modeled, and experimentally characterized a planar geometry for the investigation of nonlocal spatial solitons in a tunable reorientational medium such as voltage-controlled nematic liquid crystals. By employing interdigitated comb electrodes deposited on each side of the cell we were able to mimic an effective anchoring dependent on an external applied voltage. At variance with previous NLC samples and experiments, we were able to decouple nonlinearity and nonlocality, the former depending on applied bias and the latter on the smallest cell dimension, respectively. We found a perfect match between director distributions calculated at a given voltage, either with a Green function formalism or numerically. We derived a theoretical expression for the equivalent Kerr coefficient in nonlinear dielectrics which are nonlocal in both transverse and longitudinal coordinates with respect to a propagating light beam. An equivalent 2D model was derived which retains the main features of the complete 3D model but requires much shorter computation times. To compare model and experimental results for soliton propagation versus nonlinearity, we determined soliton waist and trajectory in the highly nonlocal case and found an excellent agreement between data and theory. We verified experimentally the predicted soliton self-steering via nonlinear changes in walk-off and in various anchoring conditions.

Our findings are relevant to nonlinear light self-confinement in the presence of nonlocality and demonstrate an adjustable nonlinear configuration for nematicons. Further investigations will deal with interactions between solitons and between solitons and defects, pinpointing the role of nonlocality as well as of nonlinearity. Finally, the presented novel geometry entails reconfigurable interconnects, whereby optically induced waveguides corresponding to individual solitons can be used as signal steering elements with deflections depending on both applied bias and light power, without the detrimental effects of out-of-plane walk-off.

ACKNOWLEDGMENT

We thank A. Dyadyusha for precious help with the samples.

APPENDIX: CALCULATION OF THE INTEGRALS INVOLVED IN ELECTRICALLY DRIVEN DIRECTOR REORIENTATION

From Eq. (22) it is easy to find that

$$R(m) = \frac{\sin\phi - e^{-\kappa L}\sin\left(\frac{\pi m}{2}\right)\cos\phi}{\sqrt{\left(\frac{\pi m}{L}\right)^2 + 4\kappa^2}}, \tag{A1}$$

with $\phi = \arctan(\frac{\pi m}{2\kappa L})$. For $p = 0$ Eq. (21) gives

$$Q(z,0,m) = \begin{cases} \frac{L}{\pi m}\left(2 - e^{-\frac{\pi m}{L}z} - e^{-\frac{\pi m}{L}[(\Lambda - l) - z]}\right), & 0 < z < (\Lambda - l), \\ \frac{L}{\pi m}e^{-\frac{\pi m}{L}z}\left[e^{\frac{\pi m}{L}(\Lambda - l)} - 1\right], & z \geqslant (\Lambda - l). \end{cases} \tag{A2}$$

For $p < 0$,

$$Q(z,p,m) = \frac{L}{\pi m}e^{-\frac{\pi m}{L}z + \frac{\pi m}{L}p\Lambda}\left[e^{\frac{\pi m}{L}(\Lambda - l)} - 1\right], \tag{A3}$$

and for $p > 0$,

$$Q(z,p,m) = \frac{L}{\pi m}e^{\frac{\pi m}{L}z - \frac{\pi m}{L}p\Lambda}\left[1 - e^{-\frac{\pi m}{L}(\Lambda - l)}\right]. \tag{A4}$$

Noteworthy, only the coefficients R depend on the coupling coefficient κ, as expected.

[1] T. Dauxois and M. Peyrard, *Physics of Solitons* (Cambridge University Press, Cambridge, 2006).

[2] Y. S. Kivshar and G. P. Agrawal, *Optical Solitons* (Academic, San Diego, 2003).

[3] C. Conti and G. Assanto, in *Encyclopedia of Modern Optics* (Elsevier, Oxford, 2004), pp. 43–55.

[4] G. Assanto and G. Stegeman, Opt. Express **10**, 388 (2002).

[5] R. Y. Chiao, E. Garmire, and C. H. Townes, Phys. Rev. Lett. **13**, 479 (1964).

[6] G. C. Duree, J. L. Shultz, G. J. Salamo, M. Segev, A. Yariv, B. Crosignani, P. Di Porto, E. J. Sharp, and R. R. Neurgaonkar, Phys. Rev. Lett. **71**, 533 (1993).

[7] W. E. Torruellas, Z. Wang, D. J. Hagan, E. W. VanStryland, G. I. Stegeman, L. Torner, and C. R. Menyuk, Phys. Rev. Lett. **74**, 5036 (1995).

[8] M. T. G. Canva, R. A. Fuerst, S. Baboiu, G. I. Stegeman, and G. Assanto, Opt. Lett. **22**, 1683 (1997).

[9] G. Leo, L. Colace, A. Amoroso, A. Di Falco, and G. Assanto, Opt. Lett. **28**, 1031 (2003).

[10] G. Leo, A. Amoroso, L. Colace, G. Assanto, R. V. Roussev, and M. M. Fejer, Opt. Lett. **29**, 1778 (2004).

[11] K. Gallo, A. Pasquazi, S. Stivala, and G. Assanto, Phys. Rev. Lett. **100**, 053901 (2008).

[12] F. Derrien, J. F. Henninot, M. Warenghem, and G. Abbate, J. Opt. A: Pure Appl. Opt. **2**, 332 (2000).

[13] C. Rotschild, O. Cohen, O. Manela, M. Segev, and T. Carmon, Phys. Rev. Lett. **95**, 213904 (2005).

[14] M. Peccianti, A. De Rossi, G. Assanto, A. De Luca, C. Umeton, and I. C. Khoo, Appl. Phys. Lett. **77**, 7 (2000).

[15] M. A. Karpierz, Phys. Rev. E **66**, 036603 (2002).

[16] G. Assanto and M. Peccianti, IEEE J. Quantum Electron. **39**, 13 (2003).

[17] C. Conti, M. Peccianti, and G. Assanto, Phys. Rev. Lett. **91**, 073901 (2003).

[18] C. Conti, M. Peccianti, and G. Assanto, Phys. Rev. Lett. **92**, 113902 (2004).

[19] M. Peccianti and G. Assanto, Opt. Lett. **26**, 1690 (2001).

[20] M. Peccianti, C. Conti, G. Assanto, A. De Luca, and C. Umeton, Nature **432**, 733 (2004).

[21] A. Alberucci, M. Peccianti, G. Assanto, G. Coschignano, A. De Luca, and C. Umeton, Opt. Lett. **30**, 1381 (2005).

[22] M. Peccianti, A. Dyadyusha, M. Kaczmarek, and G. Assanto, Nature Phys. **2**, 737 (2006).

[23] A. Alberucci and G. Assanto, J. Opt. Soc. Am. B **24**, 2314 (2007).

[24] M. Peccianti, C. Conti, G. Assanto, A. De Luca, and C. Umeton, Appl. Phys. Lett. **81**, 3335 (2002).

[25] S. V. Serak, N. V. Tabiryan, M. Peccianti, and G. Assanto, IEEE Photon. Techn. Lett. **18**, 1287 (2006).

[26] A. Piccardi, A. Alberucci, U. Bortolozzo, S. Residori, and G. Assanto, IEEE Photon. Techn. Lett. **22**, 694 (2010).

[27] M. Peccianti, C. Conti, and G. Assanto, Opt. Lett. **30**, 415 (2005).

[28] G. Assanto, M. Peccianti, and C. Conti, Opt. Photon. News **14**, 44 (2003).

[29] M. Peccianti, C. Conti, and G. Assanto, Opt. Lett. **28**, 2231 (2003).

[30] W. Hu, T. Zhang, Q. Guo, L. Xuan, and S. Lan, Appl. Phys. Lett. **89**, 071111 (2006).

[31] C. Conti, M. Peccianti, and G. Assanto, Opt. Lett. **31**, 2030 (2006).

[32] A. Fratalocchi, G. Assanto, K. Brzdakiewicz, and M. Karpierz, Opt. Express **13**, 1808 (2005).

[33] G. Assanto, A. Fratalocchi, and M. Peccianti, Opt. Express **15**, 5248 (2007).

[34] F. Ye, Y. V. Kartashov, and L. Torner, Phys. Rev. A **76**, 033812 (2007).

[35] M. Peccianti, G. Assanto, A. Dyadyusha, and M. Kaczmarek, Phys. Rev. Lett. **98**, 113902 (2007).

[36] J. Beeckman, H. Azarinia, and M. Haelterman, Opt. Lett. **34**, 1900 (2009).

[37] A. Piccardi, M. Peccianti, G. Assanto, A. Dyadyusha, and M. Kaczmarek, Appl. Phys. Lett. **94**, 091106 (2009).

[38] A. W. Snyder and D. J. Mitchell, Science **276**, 1538 (1997).

[39] M. Peccianti and G. Assanto, Opt. Lett. **30**, 2290 (2005).

[40] A. Piccardi, A. Alberucci, and G. Assanto, Appl. Phys. Lett. **96**, 061105 (2010).

[41] Y. V. Izdebskaya, V. G. Shvedov, A. S. Desyatnikov, W. Z. Krolikowski, M. Belic, G. Assanto, and Y. S. Kivshar, Opt. Express **18**, 3258 (2010).

[42] B. Alfassi, C. Rotschild, O. Manela, M. Segev, and D. N. Christodoulides, Opt. Lett. **32**, 154 (2006).

[43] A. Alberucci, M. Peccianti, and G. Assanto, Opt. Lett. **32**, 2795 (2007).

[44] D. N. Christodoulides and T. H. Coskun, Opt. Lett. **21**, 1220 (1996).

[45] M. Shih, P. Leach, M. Segev, M. H. Garrett, G. Salamo, and G. C. Valley, Opt. Lett. **21**, 324 (1996).

[46] W. E. Torruellas, Z. Wang, L. Torner, and G. I. Stegeman, Opt. Lett. **20**, 1949 (1995).

[47] W. E. Torruellas, G. Assanto, B. L. Lawrence, R. A. Fuerst, and G. I. Stegeman, Appl. Phys. Lett. **68**, 1449 (1996).

[48] A. V. Mamaev, M. Saffman, D. Z. Anderson, and A. A. Zozulya, Phys. Rev. A **54**, 870 (1996).

[49] Y. V. Kartashov, V. A. Vysloukh, and L. Torner, Opt. Lett. **34**, 1543 (2009).

[50] P. Courteille, R. S. Freeland, D. J. Heinzen, F. A. van Abeelen, and B. J. Verhaar, Phys. Rev. Lett. **81**, 69 (1998).

[51] S. E. Pollack, D. Dries, M. Junker, Y. P. Chen, T. A. Corcovilos, and R. G. Hulet, Phys. Rev. Lett. **102**, 090402 (2009).

[52] C. Daraio, V. F. Nesterenko, E. B. Herbold, and S. Jin, Phys. Rev. E **73**, 026610 (2006).

[53] N. Tabiryan and B. Zeldovich, Mol. Cryst. Liq. Cryst. **62**, 237 (1980).

[54] I. C. Khoo, *Liquid Crystals: Physical Properties and Nonlinear Optical Phenomena* (Wiley, New York, 1995).

[55] C. Conti, A. Fratalocchi, M. Peccianti, G. Ruocco, and S. Trillo, Phys. Rev. Lett. **102**, 083902 (2009).

[56] D. Suter and T. Blasberg, Phys. Rev. A **48**, 4583 (1993).

[57] C. Conti, G. Ruocco, and S. Trillo, Phys. Rev. Lett. **95**, 183902 (2005).

[58] D. W. McLaughlin, D. J. Muraki, M. J. Shelley, and X. Wang, Physica D **88**, 55 (1995).

[59] N. Ghofraniha, C. Conti, G. Ruocco, and S. Trillo, Phys. Rev. Lett. **99**, 043903 (2007).

[60] P. G. DeGennes and J. Prost, *The Physics of Liquid Crystals* (Oxford Science, New York, 1993).

[61] F. Simoni, *Nonlinear Optical Properties of Liquid Crystals* (World Scientific, Singapore, 1997).

[62] C. Conti, M. Peccianti, and G. Assanto, Phys. Rev. E **72**, 066614 (2005).

[63] W. Krolikowski and O. Bang, Phys. Rev. E **63**, 016610 (2000).

[64] O. Bang, W. Krolikowski, J. Wyller, and J. J. Rasmussen, Phys. Rev. E **66**, 046619 (2002).

[65] M. Segev, G. C. Valley, B. Crosignani, P. DiPorto, and A. Yariv, Phys. Rev. Lett. **73**, 3211 (1994).

[66] I. Kaminer, C. Rotschild, O. Manela, and M. Segev, Opt. Lett. **32**, 3209 (2007).

[67] Z. Xu, Y. V. Kartashov, and L. Torner, Phys. Rev. Lett. **95**, 113901 (2005).

[68] S. Ouyang, Q. Guo, and W. Hu, Phys. Rev. E **74**, 036622 (2006).

[69] G. B. Arfken and H. J. Weber, *Mathematical Methods for Physicists* (Academic, New York, 2001).

[70] S. K. Turitsyn, Theor. Math. Phys. **64**, 797 (1985).

[71] A. Alberucci and G. Assanto, J. Nonlinear Opt. Phys. Mater. **16**, 295 (2007).

[72] A. Alberucci, A. Piccardi, U. Bortolozzo, S. Residori, and G. Assanto, Opt. Lett. **35**, 390 (2010).

[73] W. H. Press, B. P. Flannery, S. A. Teukolsky, and W. T. Vetterling, *Numerical Recipes in C, the Art of Scientific Computing* (Cambridge University Press, Cambridge, 1992).

[74] M. Peccianti, A. Fratalocchi, and G. Assanto, Opt. Express **12**, 6524 (2004).